https://doi.org/10.5194/egusphere-2026-6598
Preprint. Discussion started: 23 November 2026
© Author(s) 2026. CC BY 4.0 License.

Evolution of cloud-top radiative cooling and entrainment during Arctic cold air outbreaks

Michael Schäfer[1], André Ehrlich[1], Evelyn Jäkel[1], Benjamin Kirbus[1,*], Joshua J. Müller[1], Sophie Rosenburg[1], Matthew D. Shupe[2,3,4], Anna Weber[5,**], Martin Wirth[6], and Manfred Wendisch[1]

[1]Leipzig Institute for Meteorology, Leipzig University, Leipzig, Germany
[2]Cooperative Institute for Research in Environmental Sciences, University of Colorado, Boulder, CO, USA
[3]National Oceanic and Atmospheric Administration, Physical Sciences Laboratory, Boulder, CO, USA
[4]Stockholm University, Stockholm, Sweden
[5]Meteorological Institute, Ludwig–Maximilians–Universität München, Munich, Germany
[6]German Aerospace Center (DLR), Institute of Atmospheric Physics, Oberpfaffenhofen, Germany
[*]now at: Fraunhofer Institute for Energy Economics and Energy System Technology, Kassel, Germany
[**]now at: German Aerospace Center (DLR), Institute of Atmospheric Physics, Oberpfaffenhofen, Germany

Correspondence: Michael Schäfer (michael.schaefer@uni-leipzig.de)

Abstract. Cloud-top radiative cooling and entrainment influence the evolution, lifetime, and radiative impact of Arctic atmospheric boundary-layer (ABL) clouds, but remain poorly constrained during cold air outbreaks (CAOs). Direct airborne measurements are particularly challenging in supercooled cloud-top layers. Here, we combine airborne near-infrared and thermal-infrared observations with radiative-transfer simulations to investigate cloud-top radiative cooling and to obtain a radiatively derived entrainment velocity (ω_e^*). Retrieved cloud optical thickness (τ), cloud-droplet effective radius (r_{eff}), and cloud-top height (CTH) are used to reconstruct radiative cooling profiles. Their cooling magnitude and vertical distribution are combined with the observed inversion strength to estimate ω_e^*. The analysis covers an Arctic CAO characterized by a downstream transition from fragmented clouds to deeper, increasingly connected cloud fields. Median ω_e^* increases from approximately 16 mm s^{-1} to 25 mm s^{-1} along this transition. The CTH is closely associated with ω_e^*, whereas τ exhibits a positive, nonlinear relationship and r_{eff} shows a comparatively weak correlation. Distinct differences among flight legs indicate that no individual cloud property uniquely determines the radiatively derived entrainment velocity. Instead, ω_e^* reflects the combined effects of cloud structure, radiative cooling, and inversion strength. These findings highlight the importance of accounting for evolving cloud and thermodynamic conditions when assessing radiative contributions to cloud-top entrainment. The observational framework provides a basis for evaluating the representation of cloud-top radiative cooling and associated radiatively derived entrainment velocities in models of Arctic boundary-layer clouds.

1 Introduction

Low-level Arctic atmospheric boundary layer (ABL) clouds influence the radiative energy budget and lower-tropospheric stability (Shupe, 2011; Morrison et al., 2012; Wendisch et al., 2017, 2023; Becker et al., 2025; Ehrlich et al., 2025). Despite

https://doi.org/10.5194/egusphere-2026-6598
Preprint. Discussion started: 23 November 2026
© Author(s) 2026. CC BY 4.0 License.

their importance, these predominantly mixed-phase clouds are poorly represented in Arctic climate projections owing to their complex interactions with atmospheric radiation and ABL turbulence (Wood, 2012; Wendisch et al., 2023; Ceppi et al., 2024).

Arctic marine cold air outbreaks (CAOs) provide a natural laboratory for studying coupled cloud–radiation–turbulence interactions under rapidly evolving ABL conditions in terms of time and space. During CAOs, cold air masses are advected from the sea ice over warm open ocean, inducing strong surface energy fluxes of heat and moisture, ABL deepening, cloud formation, and substantial air-mass transformation (Gryschka et al., 2014; Kirbus et al., 2023, 2024; Wendisch et al., 2024, 2025). The associated cloud fields typically evolve from shallow, broken cloud streets near the sea-ice edge towards more closed and optically thicker cloud decks downstream (Brümmer, 1999; Gryschka et al., 2008; Klingebiel et al., 2025). These transitions occur over small spatial and temporal scales and are accompanied by changes in cloud organization, radiative cooling, and turbulent mixing. In CAOs, clouds exhibit strong horizontal variability in their macrophysical and radiative properties on scales ranging from several kilometers down to a few tens of meters (Gryschka et al., 2014; Klingebiel et al., 2025).

A central process controlling the development, lifetime, and radiative impact of ABL clouds is cloud-top entrainment, defined as the mixing of free-tropospheric air into the cloud top layer (Lilly, 1968; Stevens, 2002; Mellado, 2017). Entrainment influences cloud geometric and optical thickness, liquid water path, cloud fraction, and cloud-top height (CTH), thereby modifying cloud and precipitation evolution and radiative properties (Bretherton and Wyant, 1997; Wood, 2012). However, entrainment emerges from the interaction of radiative cooling, buoyancy generation, inversion strength, cloud structure, and mechanical forcing (Shupe et al., 2013; Morrison et al., 2012; Neggers et al., 2025). The relative importance of these controls depends strongly on the cloud regime. Recent large-eddy simulations of Arctic mixed-phase clouds, for example, demonstrate that entrainment efficiency can be substantially enhanced by surface coupling and local wind shear (Neggers et al., 2025). In broken and optically thin cloud fields, entrainment is more strongly influenced by local radiative effects and small-scale cloud heterogeneity, whereas in more stratiform and optically thicker cloud layers, CTH and cloud optical thickness (τ) impose stronger constraints on entrainment (Bretherton and Wyant, 1997; Sedlar et al., 2012; Mellado, 2017).

Despite its importance, cloud-top entrainment is difficult to observe, particularly in Arctic ABL clouds with super-cooled liquid water layers that may cause icing of instrument platforms used for the in-situ measurements (Lloyd et al., 2015). Consequently, observational studies tend to rely on indirect diagnostics, budget approaches, model-based proxies, or novel satellite-based retrieval techniques (Mitra and Ghate, 2026). Cloud-top radiative cooling is estimated from radiative transfer simulations (Turner et al., 2018; Zheng et al., 2021; Ren et al., 2023) while in-situ observations remain sparse (Chechin et al., 2023; La et al., 2025). Methods applying tethered-balloon profiling (Egerer et al., 2019) provide meter-scale vertical resolution also in super-cooled liquid cloud tops, but are often limited by the length of the tether and restricted to the clouds above a fixed measurement site (e.g., Egerer et al., 2019; Lonardi et al., 2022, 2024). Aircraft-based observations yield spatially extensive sampling of Arctic ABL cloud systems. Coupled with radiative transfer simulations, they enable cloud-top radiative cooling to be quantified over much larger spatial scales than is possible from tethered-balloon observations, thereby facilitating the investigation of its role in radiatively induced entrainment-like processes.

Here, radiatively driven cloud-top entrainment in Arctic CAO clouds is investigated by imaging remote sensing from the High Altitude And Long Range research aircraft (HALO, Krautstrunk and Giez, 2012) during the airborne $(\mathcal{AC})^3$ (ArctiC Am-

https://doi.org/10.5194/egusphere-2026-6598
Preprint. Discussion started: 23 November 2026
© Author(s) 2026. CC BY 4.0 License.

plification: Climate Relevant Atmospheric and SurfaCe Processes, and Feedback Mechanisms) campaign called HALO-$(\mathcal{AC})^3$ (Wendisch et al., 2024; Ehrlich et al., 2025). From the high-resolution airborne imaging, dropsonde measurements, and radiative-transfer simulations, cloud microphysical and macrophysical properties are obtained, which are translated into radiative cooling diagnostics. From this, a radiatively constrained entrainment proxy, the so-called radiatively derived entrainment velocity ω_e^*, is derived. This proxy characterizes the radiative and inversion-modulated contribution to entrainment-like dynamics rather than the direct entrainment rate. The observations capture the downstream evolution of CAO clouds from fragmented, optically thin cloud fields, towards increasingly closed and optically thicker cloud decks. They provide an observational perspective on how cloud-state-dependent radiation–turbulence coupling evolves during Arctic CAO development.

Section 2 introduces the observational data, retrieval framework, and radiative-transfer simulations. Section 3 presents the downstream evolution of cloud structure and radiative diagnostics across the four flight legs, while Sect. 4 examines the bivariate relationships between ω_e^* and selected cloud properties. The main conclusions and implications are summarized in Sect. 5.

2 Data and methods

2.1 Campaign and flight strategy

During HALO-$(\mathcal{AC})^3$ (Wendisch et al., 2024), HALO was operated from Kiruna, northern Sweden. In total, 17 research flights (RF) were performed over the Fram Strait and into the high Arctic, covering different states of warm air intrusions and CAOs. The observations analysed here were collected during research flight 10 (RF10) on 29 March 2022. During the first flight section of RF10, CAO conditions were sampled south and southeast of Svalbard along a sequence of downstream flight legs representing successive stages of Arctic CAO cloud-field evolution (Walbröl et al., 2024; Wendisch et al., 2025).

The flight track and corresponding air mass trajectories are shown in Fig. 1. A true-color reflectance composite from the Moderate Resolution Imaging Spectroradiometer (MODIS, Platnick et al., 2003) operated onboard the Terra satellite is shown in the background to illustrate the large-scale cloud distribution and sea-ice edge (cyan line). As the reflectance product represents a daily composite, the cloud structures do not necessarily coincide exactly with the instantaneous aircraft observations, but provide qualitative context for the prevailing cloud regime.

The four flight legs are highlighted in distinct colors. To avoid contamination by a cirrus layer in the eastern part, only the western sections of the four parallel flight legs are considered in the analysis. For each leg, 24-hour backward trajectories are computed using the Lagrangian Analysis Tool (LAGRANTO, Sprenger and Wernli, 2015) and initialized every minute along the flight track at approximately CTH. The trajectories illustrate that the CAO developed from Leg 4 to Leg 1. Although the flight strategy was not quasi-Lagrangian, the individual legs sample different regions of the CAO, from fragmented cloud fields near the upstream sea-ice edge to deeper and increasingly connected clouds farther downstream.

While Leg 4 was sampled in the immediate vicinity of the sea-ice edge, the representative air masses sampled during Legs 3, 2, and 1 had spent approximately 1.6 h, 2.2 h, and 4.2 h over open ocean, respectively (time since last crossing of the 15 % sea-ice concentration derived from the Advanced Microwave Scanning Radiometer - 2, AMSR2 (Spreen et al., 2008)).

https://doi.org/10.5194/egusphere-2026-6598
Preprint. Discussion started: 23 November 2026
© Author(s) 2026. CC BY 4.0 License.

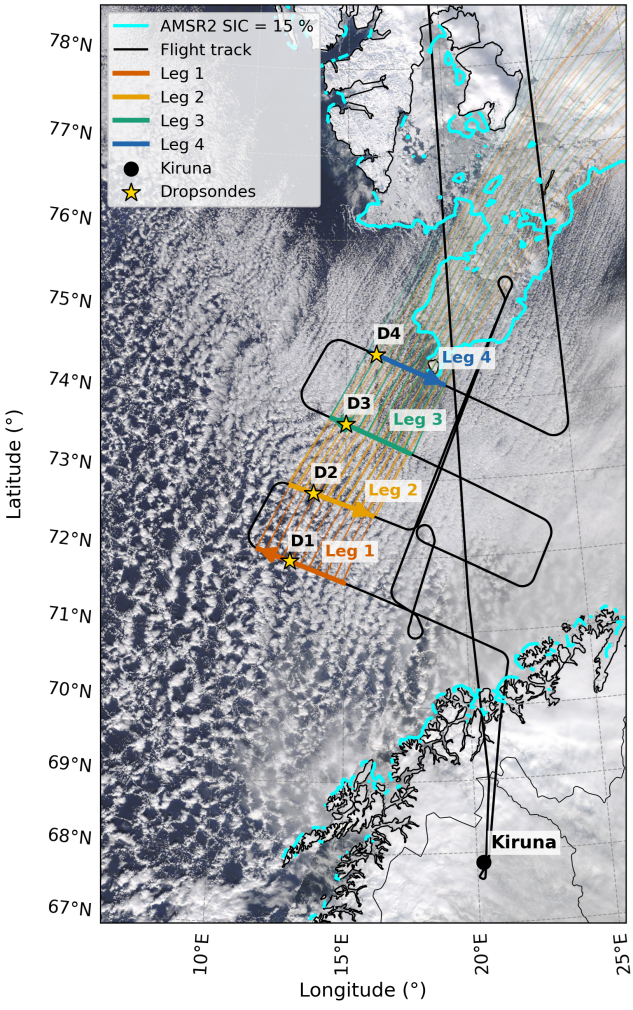

Figure 1. Flight track and backward trajectories for the HALO-$(\mathcal{AC})^3$ case study south of Svalbard during RF10 on 29 March 2022. The analysed western sections of the four flight legs are indicated along the aircraft track. Air mass backward trajectories are coloured according to the flight leg during which they were started. The background imagery is based on MODIS Corrected Reflectance (Bands 1–4–3) derived from Level-1B products MOD02QKM, MOD02HKM, and MOD021KM provided through NASA Worldview/GIBS. Dropsonde locations are indicated by star symbols. The cyan contour indicates the 15 % sea-ice concentration threshold derived from AMSR2 (Spreen et al., 2008).

For each flight leg, one nearby dropsonde measurement (George et al., 2024) is selected to provide representative thermodynamic context for the analysed western section of the cloud field. The corresponding vertical profiles of potential temperature (θ), relative humidity (RH), and specific humidity (q) are shown in Fig. 2. The inversion height is identified from the maximum vertical gradient in θ within a leg-specific altitude range. Using virtual potential temperature (θ_v) instead yields the same inversion height for all four representative profiles, indicating that the inversion identification is insensitive to the inclu-

https://doi.org/10.5194/egusphere-2026-6598
Preprint. Discussion started: 23 November 2026
© Author(s) 2026. CC BY 4.0 License.

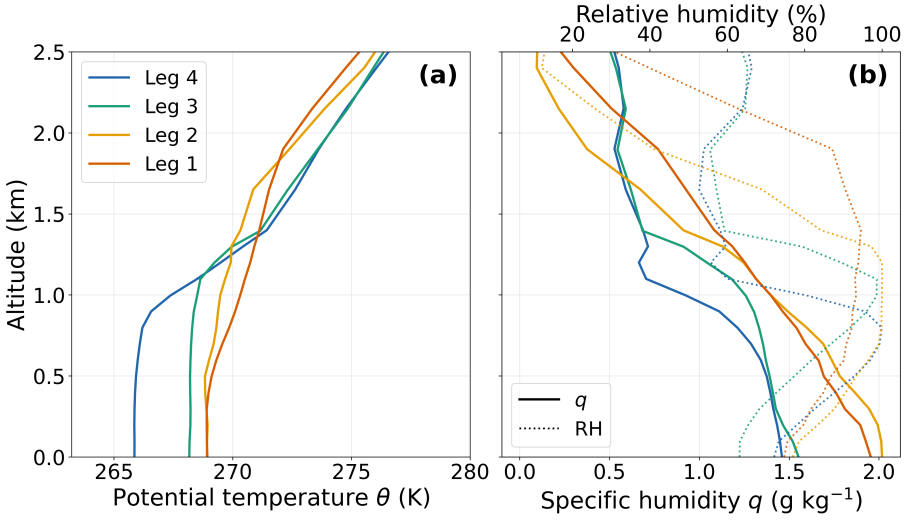

Figure 2. Thermodynamic profiles derived from the dropsonde observations selected as representative of the analysed western sections of the four flight legs on 29 March 2022. Shown are **(a)** potential temperature and **(b)** specific humidity and relative humidity.

sion of the moisture correction for θ. The selected profiles indicate a progressive warming and deepening of the marine ABL across the downstream sequence of the four flight legs, from approximately 1.0 km in Leg 4 to about 2.0 km in Leg 1, together with a moister and more vertically extended humid layer. Additional dropsondes released during RF10 are used to assess the spatial representativeness of the selected profiles. Soundings that sample comparable parts of the cloud field show consistent thermodynamic structure, whereas larger differences occur for soundings located farther along the eastern extensions of the flight legs. Overall, the representative profiles are consistent with an evolving CAO ABL, in which cloud deepening, moisture redistribution, and gradual changes in stability accompany the transition from fragmented upstream clouds towards deeper and increasingly connected cloud fields downstream.

2.2 Airborne imaging observations

The cloud fields are characterized using airborne imaging observations that provide data with high spatial resolution (about 10 m pixel size), capturing the small-scale structure of the clouds. Different spectral bands are used to retrieve cloud properties, including τ, cloud-droplet effective radius (r_{eff}) at cloud top, and CTH. These observations and retrieved properties form the basis for the subsequent derivation and analysis of radiative heating rates (ζ) and radiatively derived entrainment velocity ω_{e}^{*}.

Figure 3a illustrates the high-resolution pushbroom observations of near-infrared reflectivity (R). The near-infrared measurements (1000–2500 nm) are acquired by the spectrometer of the Munich Aerosol Cloud Scanner (specMACS, Ewald et al., 2016), providing spatially resolved spectral radiances I_λ (in units of W m^{-2} nm^{-1} sr^{-1}) available from Weber et al. (2024b). In Fig. 3a, to account for variations in solar illumination geometry during the flight, the measured radiance at 1250 nm is converted to reflectivity according to:

https://doi.org/10.5194/egusphere-2026-6598
Preprint. Discussion started: 23 November 2026
© Author(s) 2026. CC BY 4.0 License.

$$R_{1250} = \frac{\pi I_{1250}}{F^{\downarrow}_{1250}}, \tag{1}$$

where I_{1250} is the measured spectral radiance and $F^{\downarrow}_{1250}$ is the simulated downward solar spectral irradiance at flight altitude for the specMACS 1250 nm channel. This effective downward irradiance, $F^{\downarrow}_{1250}$, is obtained by weighting the simulated spectrum with the spectral response of the specMACS channel. The simulation is evaluated for the specific time, location, and altitude of each observation. This normalization accounts for variations in atmospheric effects and changes in solar illumination geometry, thereby reducing differences between the flight legs.

Image data from the polarization upgrade of specMACS provide information on the dominant thermodynamic phase of cloud particles at cloud top (Weber et al., 2024a). The cloud-top phase is additionally assessed from the spectral dependence of the reflected radiation in the shortwave infrared, following the spectral-slope approach of Ehrlich et al. (2008), which exploits differences in the spectral absorption of liquid water and ice. The combined phase information indicates predominantly liquid-water-dominated cloud tops within the analyzed cloud fields, but also identifies localized signatures of ice-containing cloud tops. Since the cloud-property retrieval applied below assumes liquid-water droplets, pixels exhibiting ice signatures at cloud top are excluded from the retrieval-based analysis, as described in Sect. S1 of the Supplement. This cloud-top-based screening does not exclude the presence of ice particles deeper within the cloud layer. The phase-suspect screening excludes approximately 11.0 %, 9 %, 2 %, and 3 % of the originally identified cloudy pixels in Legs 1–4, respectively. These exclusions may introduce a sampling bias if ice-containing cloud tops are associated with systematically different cloud properties. Consequently, the derived radiative cooling and entrainment diagnostics are representative of the retained, predominantly liquid-water cloud tops rather than the entire cloud population sampled during the CAO. The impact of the excluded pixels on these diagnostics cannot be quantified within the present liquid-water retrieval framework.

Thermal-infrared brightness temperature (T_{B}) data (in units of $^{\circ}C$) are obtained from the Video airbornE Longwave Observations within siX channels (VELOX, Schäfer et al., 2022) system. The two-dimensional (2D) images are merged into pushbroom sequences similar to specMACS and provide fields of T_{B} of cloud tops and surfaces. For the four flight legs they are illustrated in Fig. 3c. The VELOX observations cover spectral bands in the wavelength range between 7.7 µm and 12 µm and are available from Schäfer et al. (2023).

The spatial observations and the corresponding histograms reveal pronounced variability among the sampled cloud fields. The histogram statistics are restricted to cloudy pixels retained for the subsequent quantitative analysis. After accounting for differences in solar illumination geometry, the median R_{1250} values range from 0.37 in Leg 1 to 0.44 in Leg 3, with similar values of 0.38 and 0.39 in Legs 2 and 4, respectively (Table 1). The brightness-temperature distributions also vary between the flight legs, with median T_{B} values of -15.5 and $-15.4\,^{\circ}$C in Legs 4 and 3 and lower values of -17.5 and $-16.8\,^{\circ}$C in Legs 2 and 1, respectively. Together with the differences in spatial cloud organization, these variations highlight distinct cloud-top characteristics among the sampled regions of the CAO.

To ensure pixel-wise spatial consistency between the near–infrared and thermal–infrared observations, the specMACS and VELOX swath data are spatially aligned. Characteristic cloud-pattern structures visible in both datasets are used to determine

https://doi.org/10.5194/egusphere-2026-6598
Preprint. Discussion started: 23 November 2026
© Author(s) 2026. CC BY 4.0 License.

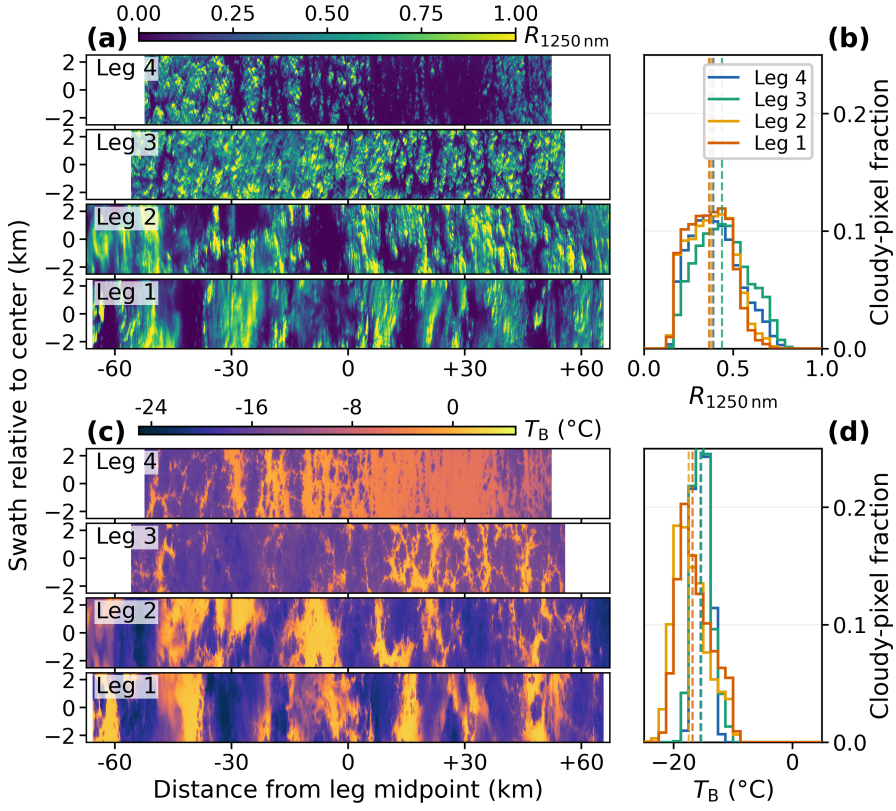

Figure 3. Pushbroom images of **(a)** specMACS reflectivity R_{1250} and **(c)** VELOX brightness temperature T_B at 7.7–12 µm for the four flight legs of 29 March 2022. The unequal scaling of the across- and along-track dimensions results in partly distorted images. The corresponding histograms in **(b)** and **(d)** include only pixels retained as cloudy for the quantitative analysis (after retrieval quality control). Therefore, values visible in the images but excluded by this selection do not contribute to the histograms. Histogram frequencies are normalized by the total number of included pixels for each flight leg, such that the bin frequencies sum to unity. Dashed lines indicate the median values and may overlap where medians are similar. The x-axis spans the same value range as the respective color bar. Median values are summarized in Table 1.

relative spatial offsets between the instruments. The swaths are then shifted accordingly and interpolated onto a common spatial grid. This approach allows the observations of R_{1250} and T_B to be used jointly.

A cloud mask is derived from the original specMACS radiance observations by classifying all pixels with I_{1250} exceeding 0.005 W m^{-2} nm^{-1} sr^{-1} as cloudy. The resulting cloud mask is applied uniformly to all datasets to ensure pixel-wise consistency between the observed quantities, retrieved cloud properties, and derived radiative quantities.

https://doi.org/10.5194/egusphere-2026-6598
Preprint. Discussion started: 23 November 2026
© Author(s) 2026. CC BY 4.0 License.

2.3 Radiative diagnostics and entrainment framework

The purpose of the following framework is to relate the simulated cloud-top radiative cooling to a diagnostic measure of its potential contribution to cloud-top entrainment. Rather than estimating the actual entrainment rate, we define a radiatively derived entrainment velocity ω_e^*, representing the exchange velocity that would be required to offset the simulated cloud-top radiative cooling across the observed inversion.

Classical mixed-layer budget formulations relate entrainment-induced warming to the entrainment velocity, the inversion strength, and a characteristic vertical length scale of the mixed layer (Lilly, 1968; Stevens, 2002; Morrison et al., 2012; Mellado, 2017). A conceptually related thermodynamic approach, which balances radiative heating with buoyancy-driven vertical displacement, was applied to aerosol layers by Boers et al. (2010). In their framework, radiative heating produces a diabatic potential-temperature tendency, which is translated into a vertical displacement according to the static stability of the surrounding atmosphere. Here, we apply an analogous bulk argument with opposite sign to radiative cooling at cloud top. Rather than describing the displacement of a heated layer through a continuously stratified atmosphere, we characterize the thermodynamic resistance to vertical exchange by the finite potential-temperature jump across the cloud-top inversion, $\Delta\theta_{\mathrm{inv}}$.

Following the thermodynamic displacement argument of Boers et al. (2010), we approximate the effective bulk stability relevant to radiatively driven vertical exchange as $\Delta\theta_{\mathrm{inv}}/z_c$, where z_c is a characteristic depth of the simulated cloud-top cooling distribution. This adaptation replaces the continuous ambient potential-temperature gradient used by Boers et al. (2010) with a bulk measure based on the cloud-top inversion strength. The resulting radiatively derived entrainment velocity is then defined as:

$$\omega_e^* \equiv \frac{|\zeta_{20\,\mathrm{m}}|/3600}{\Delta\theta_{\mathrm{inv}}/z_c} = \frac{z_c}{3600}\frac{|\zeta_{20\,\mathrm{m}}|}{\Delta\theta_{\mathrm{inv}}}. \tag{2}$$

Here, $\zeta_{20\,\mathrm{m}}$ is the mean radiative potential-temperature tendency within the uppermost 20 m of the cloud layer, expressed in K h^{-1}, z_c is expressed in m, and $\Delta\theta_{\mathrm{inv}}$ in K, such that ω_e^* has units of $\mathrm{m\,s}^{-1}$. The 20 m averaging depth is motivated by the characteristic radiative extinction length ($\lambda \approx 10$–20 m) reported for continuous, optically thick stratiform clouds by Mellado (2017). The diagnostic is associated with the cloud-top interface but is not evaluated at a specific altitude or model level. In particular, the uppermost 20 m defines the layer over which the radiative cooling rate is averaged, while z_c provides a characteristic vertical length scale rather than the altitude at which ω_e^* applies. The quantities entering this definition are introduced below.

The inversion strength $\Delta\theta_{\mathrm{inv}}$ is defined as the potential-temperature difference across the inversion layer and is derived from the representative dropsonde profile associated with each flight leg. Because only one representative dropsonde profile is available for each flight leg, $\Delta\theta_{\mathrm{inv}}$ is treated as constant within the respective leg. The assumption of a constant $\Delta\theta_{\mathrm{inv}}$ within each leg introduces uncertainty in the magnitude of ω_e^*. For illustration, a $\pm 10\,\%$ change in $\Delta\theta_{\mathrm{inv}}$ results in a -9 % to +11 % change in ω_e^*. While uniform changes only rescale the proxy, unresolved within-leg variations may also affect its spatial distribution.

https://doi.org/10.5194/egusphere-2026-6598
Preprint. Discussion started: 23 November 2026
© Author(s) 2026. CC BY 4.0 License.

The remaining quantities entering Eq. (2), namely $\zeta_{20\,\mathrm{m}}$ and z_c, are derived from radiative-transfer simulations based on reconstructed cloud profiles described in Sect. S3 of the Supplement and summarized in Sect. 2.4. These simulations provide vertical profiles of upward and downward broadband radiative flux densities, $F^{\uparrow}(z)$ and $F^{\downarrow}(z)$, from which the radiative tendencies and cloud-top cooling diagnostics are derived. The net radiative flux density is defined as:

$$F_\mathrm{net}(z) = F^{\downarrow}(z) - F^{\uparrow}(z). \tag{3}$$

With this sign convention, positive values represent a net downward flux. Figure 4a schematically illustrates the vertical structure of the net radiative flux near cloud top. The corresponding radiative temperature tendency is obtained from the vertical divergence of this flux:

$$\zeta_T(z) = -\frac{1}{\rho(z)\cdot c_\mathrm{p}}\frac{\partial F_\mathrm{net}(z)}{\partial z}, \tag{4}$$

where $\rho(z)$ is the air density at altitude z and $c_\mathrm{p} = 1004\ \mathrm{J\,kg^{-1}\,K^{-1}}$ is the specific heat capacity of air. Negative values of ζ_T correspond to radiative cooling.

Because the inversion strength in Eq. (2) is expressed in terms of potential temperature, the radiative temperature tendency is converted to the corresponding potential-temperature tendency. Using $\theta = T(p_0/p)^{\kappa}$, with $\kappa = R_\mathrm{d}/c_\mathrm{p}$, where R_d=287.05 $\mathrm{J\,kg^{-1}\,K^{-1}}$ is the specific gas constant for dry air, we define the radiative potential-temperature tendency $\zeta(z)$ as:

$$\zeta(z) = \frac{\theta(z)}{T(z)}\cdot\zeta_T(z) = -\frac{\theta(z)}{T(z)}\frac{1}{\rho(z)\cdot c_\mathrm{p}}\frac{\partial F_\mathrm{net}(z)}{\partial z}. \tag{5}$$

For the low-level ABL clouds investigated here, this correction is small but is retained for thermodynamic consistency. Commonly, cloud-top cooling is dominated by terrestrial radiative flux divergence, whereas solar contributions are comparatively small.

The magnitude of cloud-top cooling is characterized by $\zeta_{20\,\mathrm{m}}$, defined as the mean radiative potential-temperature tendency within the uppermost 20 m of the cloud layer:

$$\zeta_{20\,\mathrm{m}} = \frac{1}{20\,\mathrm{m}}\int_{z_\mathrm{top}-20\,\mathrm{m}}^{z_\mathrm{top}} \zeta(z)\,\mathrm{d}z. \tag{6}$$

In a discrete model representation, the cloud-top cooling rate is calculated as the arithmetic mean of the cooling-rate values at all vertical grid points located within 20 m below cloud top. Thereby, the number of contributing grid points depends on the vertical resolution of the radiative-transfer output.

To characterize the vertical distribution of radiative cooling, the cooling centroid depth z_c is calculated from the negative contributions to the radiative potential-temperature tendency, consistent with Eq. (2):

https://doi.org/10.5194/egusphere-2026-6598
Preprint. Discussion started: 23 November 2026
© Author(s) 2026. CC BY 4.0 License.

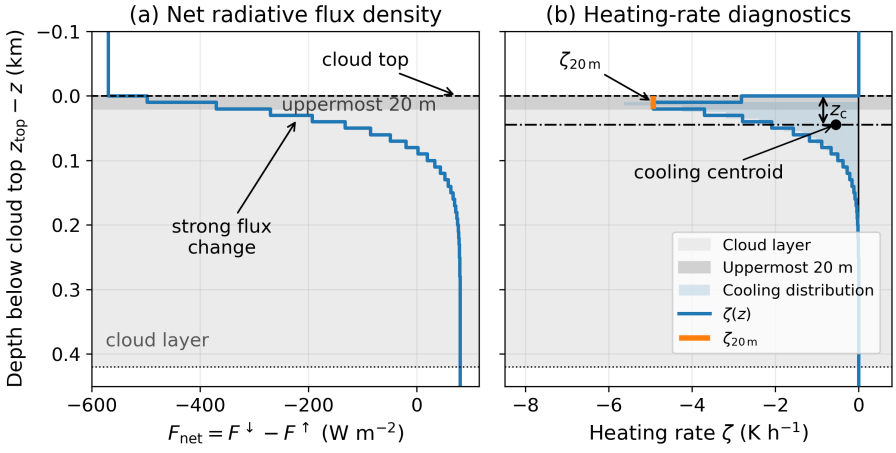

Figure 4. Illustrative example of the cloud-top radiative cooling diagnostics. **(a)** Schematic profile of net radiative flux density relative to cloud top. **(b)** Corresponding radiative potential-temperature tendency $\zeta(z)$. The shaded regions indicate the cloud layer and the uppermost 20 m used to calculate $\zeta_{20\,\mathrm{m}}$. z_c denotes the cooling-weighted centroid depth of the cooling distribution.

$$C_i = \max(0, -\zeta_i), \tag{7}$$

where the maximum operator ensures that only negative tendencies (radiative cooling) contribute to the centroid, whereas positive tendencies (radiative warming) are assigned zero weight. This does not imply that radiative warming has no dynamical effect. Rather, the centroid is specifically intended to characterize the vertical distribution of cooling-induced negative buoyancy forcing, not the net effect of radiative heating and cooling. The cooling centroid depth is then calculated as:

$$z_c = \frac{\int_{z_{base}}^{z_{top}} (z_{top} - z) \cdot C(z)\,\mathrm{d}z}{\int_{z_{base}}^{z_{top}} C(z)\,\mathrm{d}z}, \tag{8}$$

where $C(z) = \max[0, -\zeta(z)]$ denotes the magnitude of the radiative cooling tendency. Both integrals are evaluated numerically using the composite trapezoidal rule on the vertical radiative-transfer output grid. Thus, z_c represents the cooling-weighted mean distance below cloud top, considering the cooling distribution throughout the cloudy column.

Conceptually, z_c can be interpreted as the effective depth at which the vertically distributed radiative cooling acts. It is analogous to a center of mass, with the magnitude of radiative cooling replacing mass as the weighting quantity. Therefore, in Eq. (2), z_c provides the characteristic vertical length scale used to convert the inversion jump $\Delta\theta_{inv}$ into an effective bulk stability. For a vertically uniform cooling profile extending over a layer of thickness H, Eq. (8) yields $z_c = H/2$.

https://doi.org/10.5194/egusphere-2026-6598
Preprint. Discussion started: 23 November 2026
© Author(s) 2026. CC BY 4.0 License.

The relationship between the net radiative flux and the resulting radiative potential-temperature tendency is illustrated in Fig. 4. The schematic highlights how the vertical variation of the net radiative flux produces a cooling profile concentrated near cloud top. The two diagnostics describe complementary properties of this profile. $\zeta_{20\,\mathrm{m}}$ quantifies the mean cooling rate within the uppermost 20 m of the cloud, whereas z_c represents the cooling-weighted mean distance below cloud top. Consequently, two cooling profiles with similar near-cloud-top cooling rates may differ in their centroid depths if the cooling extends over different vertical distances. Through Eq. (2), these differences in cooling magnitude and vertical distribution jointly influence the radiatively derived entrainment velocity ω_e^*.

The three quantities entering Eq. (2) have distinct physical roles. The magnitude $|\zeta_{20\,\mathrm{m}}|$ characterizes the cloud-top radiative cooling, z_c provides the characteristic vertical length scale of the cooling distribution, and $\Delta\theta_\mathrm{inv}$ represents the thermodynamic resistance to entrainment across the inversion. Consequently, large values of ω_e^* occur for strong cloud-top cooling distributed over a larger cooling centroid depth acting against a weak inversion, whereas small values arise from weaker cooling, a shallower cooling distribution, or a stronger inversion.

The diagnostic is based on the simplified bulk scaling in Eq. (2) and does not explicitly account for additional processes affecting cloud-top entrainment, including shear-driven turbulence, surface forcing, subsidence, mesoscale circulations, and precipitation (Neggers et al., 2025). Although image pixels identified as phase-suspect by the retrieval quality control are excluded from the analysis, mixed-phase processes and ice particles below an apparently liquid-dominated cloud top may remain undetected. Such residual effects may locally alter radiative transfer and introduce additional uncertainty into the retrieved cloud properties and derived radiative diagnostics. Accordingly, ω_e^* is most appropriately used to compare relative differences in radiative entrainment potential rather than to quantify absolute entrainment rates. The analogy to the radiative-displacement framework of Boers et al. (2010) is restricted to the thermodynamic conversion of a radiative potential-temperature tendency into a vertical velocity and does not imply equivalent dynamical responses of cloud-top inversions and radiatively heated aerosol layers.

Uncertainties in ω_e^* are estimated by propagating measurement and retrieval uncertainties through the radiative calculations while retaining the coupled response of $\zeta_{20\,\mathrm{m}}$ and z_c, and by independently accounting for the uncertainty in $\Delta\theta_\mathrm{inv}$ (see Sect. S4 and Table S1 in the Supplement). The resulting combined median relative uncertainties range from 8.6 % to 12.3 %, corresponding to representative absolute uncertainties of approximately 1.4–2.9 mm s^{-1}.

2.4 Analysis framework

The observational and analysis framework used in this study is summarized in Fig. 5. Near-infrared radiance measurements from specMACS and thermal-infrared observations from VELOX provide the basis for retrieving cloud optical thickness (τ), cloud-droplet effective radius (r_eff), and cloud-top height (CTH). Collocated WALES observations constrain the CTH retrieval, while dropsonde measurements provide the atmospheric thermodynamic profiles. The retrieved cloud properties are used to reconstruct simplified vertical cloud profiles and perform broadband radiative-transfer simulations. The resulting heating-rate profiles are used to derive cloud-top cooling diagnostics and the radiatively derived entrainment velocity ω_e^*.

https://doi.org/10.5194/egusphere-2026-6598
Preprint. Discussion started: 23 November 2026
© Author(s) 2026. CC BY 4.0 License.

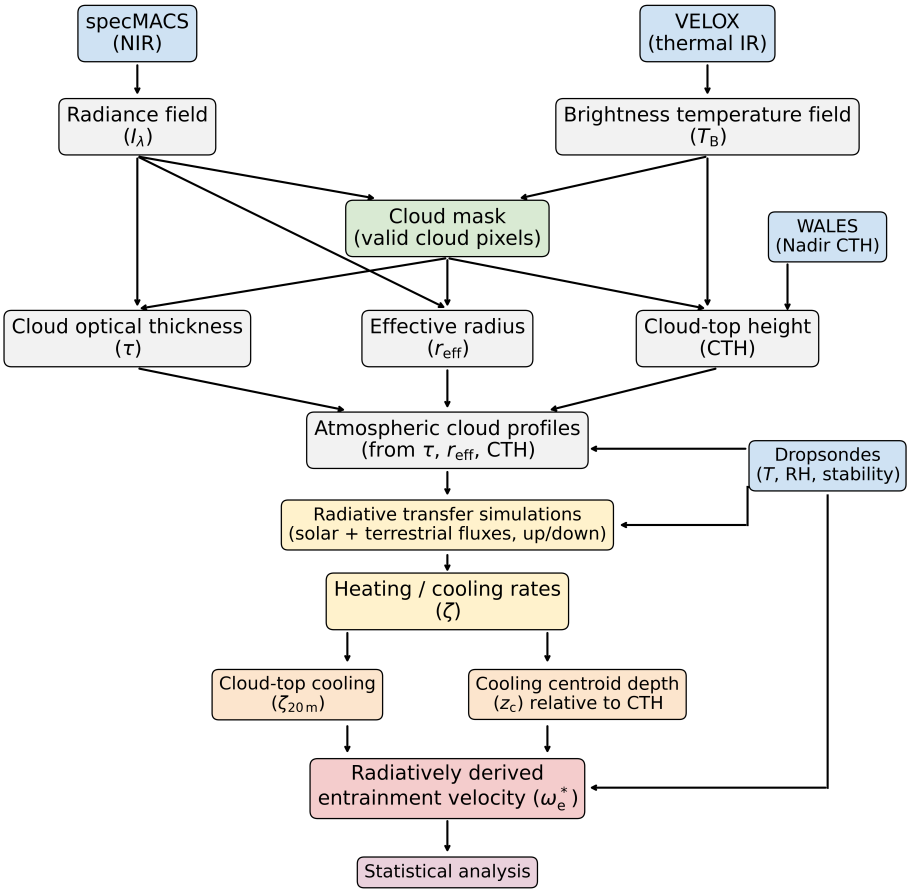

Figure 5. Schematic overview of the retrieval and analysis framework applied in this study. Airborne remote-sensing observations are used to retrieve cloud optical and geometrical properties, which provide the input for the radiative-transfer simulations. The resulting radiative flux and heating-rate profiles are subsequently used to derive the cloud-top radiative diagnostics and the radiatively derived entrainment velocity.

Figure 6 illustrates this processing chain for a representative 15 km sequence from flight Leg 2, showing the spatial distributions and corresponding frequency distributions of the observed and derived quantities. Further methodological details are provided in the Supplement, including the retrievals of cloud optical thickness and cloud-droplet effective radius (Sect. S1), cloud-top height (Sect. S2), cloud-profile reconstruction and radiative-transfer simulations (Sect. S3), and uncertainty assessment (Sect. S4).

While R_{1250} is used in Fig. 3 to compare the observed cloud fields after normalization for solar illumination geometry, the cloud-property retrieval itself operates directly on the measured absolute specMACS radiances at 1250 nm and 1600 nm. Accordingly, Fig. 6a shows the specMACS reflectivity at 1250 nm derived from the measured radiance, while Fig. 6c shows the VELOX brightness temperature in the 7.7 µm to 12 µm spectral range. The corresponding relative-frequency distributions are

https://doi.org/10.5194/egusphere-2026-6598
Preprint. Discussion started: 23 November 2026
© Author(s) 2026. CC BY 4.0 License.

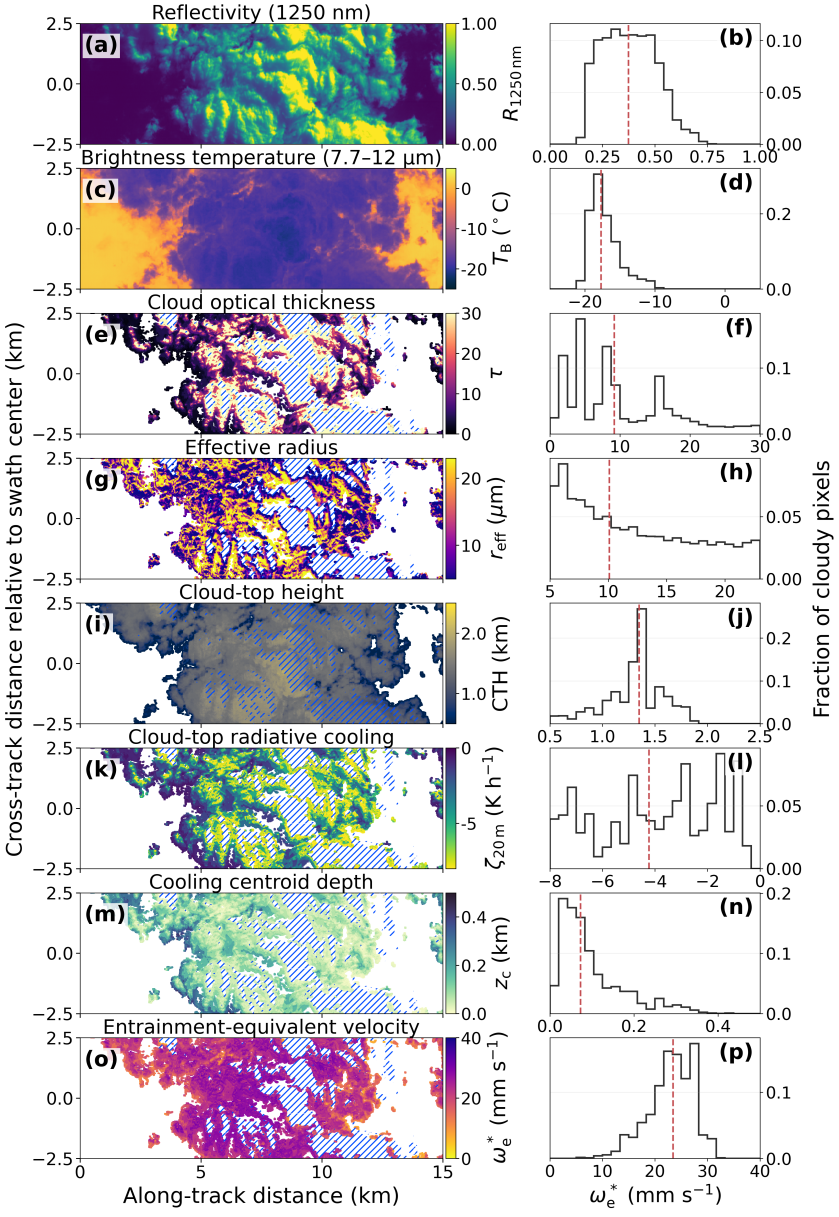

Figure 6. Example of the complete observational and analysis chain for a representative 15 km sequence from flight leg 2. Spatial distributions (left panels) and corresponding relative-frequency histograms (right panels) are shown for **(a, b)** specMACS reflectivity R_{1250}, **(c, d)** VELOX T_B, **(e, f)** retrieved τ, **(g, h)** r_{eff}, **(i, j)** CTH, **(k, l)** $\zeta_{20\,m}$, **(m, n)** z_c, and **(o, p)** ω_e^*. Dark blue hatched areas indicate cloudy pixels excluded from the quantitative analysis by the retrieval quality control, including unresolved retrieval inconsistencies, τ-saturated retrievals, and pixels flagged as potentially ice-affected. Cloud-free regions are not hatched. Histograms include only cloudy pixels retained after quality control. Dashed vertical lines indicate the median values of the corresponding quality-controlled distributions.

https://doi.org/10.5194/egusphere-2026-6598
Preprint. Discussion started: 23 November 2026
© Author(s) 2026. CC BY 4.0 License.

presented in Figs. 6b and 6d, respectively. The cloud field exhibits pronounced spatial variability, with optically thicker cloud elements corresponding to enhanced reflected solar radiance and generally lower thermal-infrared brightness temperature.

These observations form the basis for the retrieval products shown in Figs. 6(e)–(j). Regions of enhanced reflected radiance are generally associated with larger τ, while the retrieved r_{eff} reveals substantial small-scale variability that is only partly correlated with τ. The retrieved CTH indicates a comparatively shallow cloud deck with moderate horizontal variability, demonstrating that pronounced variations in cloud optical properties may occur even where CTH changes only gradually.

Using the retrieved cloud properties and the reconstructed atmospheric profiles, broadband radiative-transfer calculations are performed to derive the cloud-top radiative diagnostics shown in Figs. 6(k)–(p). Strong cloud-top radiative cooling, represented by more negative $\zeta_{20\,\mathrm{m}}$, is predominantly found in optically thicker cloud regions, whereas z_{c} exhibits a smoother spatial structure, reflecting variations in the vertical distribution of radiative cooling within the cloud layer. The resulting ω_{e}^{*} combines both diagnostics with the observed inversion strength and, therefore, highlights regions where radiative cooling is expected to provide a comparatively larger potential contribution to cloud-top entrainment.

This example illustrates how the observed spatial variability in cloud properties, together with the reconstructed atmospheric and cloud profiles, is translated through the radiative-transfer framework into diagnostics of cloud-top radiative cooling and a radiatively derived entrainment velocity.

3 Cloud evolution along the air mass trajectory

3.1 Transition from fragmented to increasingly connected cloud fields

At the upstream stage (Leg 4, Fig. 1), the cloud field is characterized by broken and spatially heterogeneous structures with low cloud fraction. Satellite imagery and airborne observations reveal typical CAO features, including cloud streets aligned with the low-level flow and pronounced mesoscale variability. Further downstream, the cloud field transitions from shallow broken clouds towards deeper and increasingly connected cloud structures.

This transition is also reflected in the thermodynamic evolution of the ABL, which is illustrated by the collocated dropsonde profiles in Fig. 2. The profiles indicate a progressive deepening of the ABL along the flow from approximately 1 km in Leg 4 to about 2.1–2.4 km in Legs 1–2, accompanied by enhanced ABL moisture and a more vertically extended humid layer.

The evolution of cloud micro- and macrophysical properties retrieved from specMACS and VELOX across the downstream sequence of the flight legs is shown in Fig. 7. The quality-controlled retrievals reveal a systematic downstream increase in CTH, with median values rising from approximately 1.00 km in Leg 4 to 1.25 km in Leg 3, 1.35 km in Leg 2, and 1.50 km in Leg 1 (Table 1). A pronounced downstream increase is also evident in r_{eff}, whose median rises from 7.4 µm in Leg 4 to 8.9 µm in Leg 3, 10.7 µm in Leg 2, and 14.6 µm in Leg 1. In contrast, τ does not exhibit a monotonic downstream evolution. Median τ is 9.1 in Leg 4, reaching a maximum of 16.0 in Leg 3, and subsequently decreasing to 9.6 and 9.4 in Legs 2 and 1, respectively. Thus, while the cloud layer progressively deepens and the retrieved droplet size increases along the trajectory, the evolution of cloud optical thickness is characterized by substantial leg-to-leg variability rather than a continuous downstream

https://doi.org/10.5194/egusphere-2026-6598
Preprint. Discussion started: 23 November 2026
© Author(s) 2026. CC BY 4.0 License.

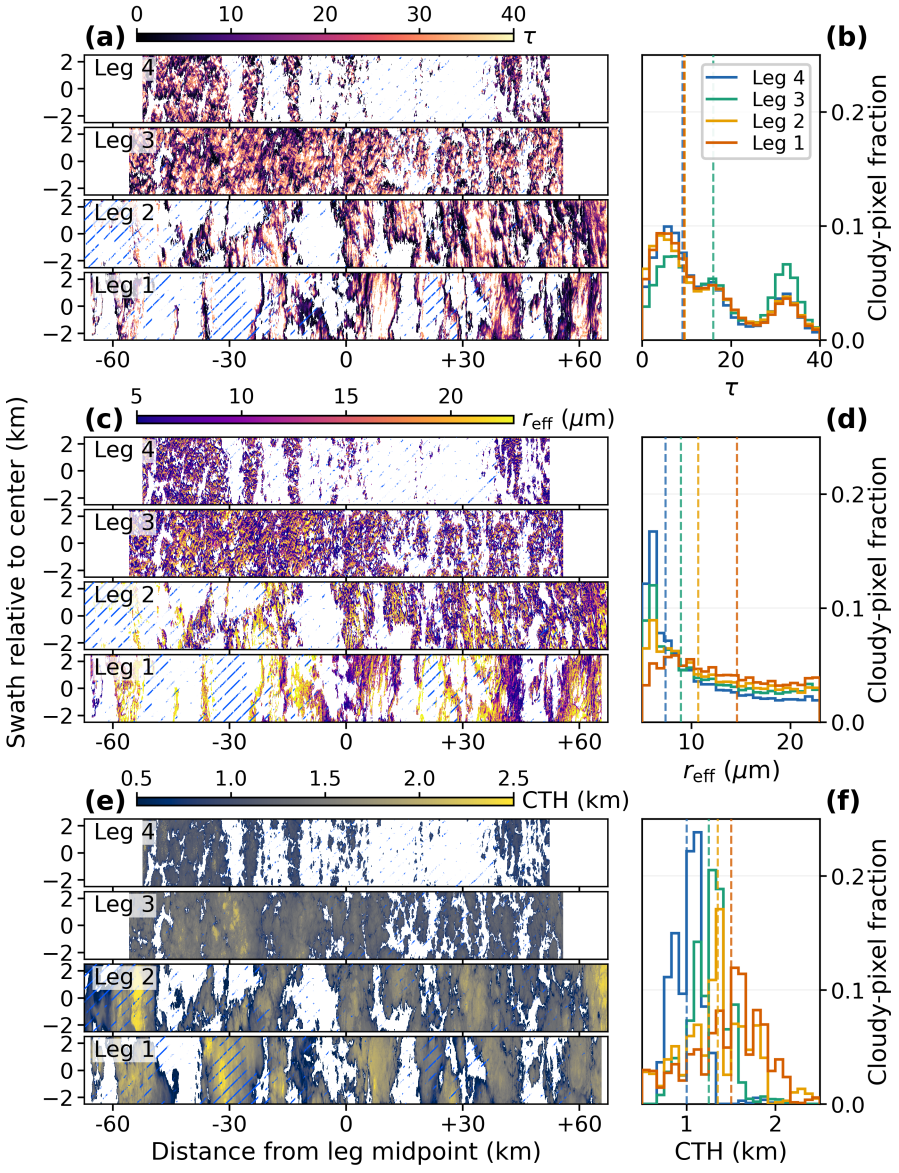

Figure 7. Like in Fig. 3, spatial distributions and corresponding relative frequency distributions of **(a, b)** τ, **(c, d)** r_{eff}, and **(e, f)** CTH, respectively. Dark blue hatched areas indicate cloudy pixels excluded from the quantitative analysis by the retrieval quality control, including unresolved retrieval inconsistencies, τ-saturated retrievals, and pixels flagged as potentially ice-affected. Cloud-free regions are not hatched. The frequency distributions include only cloudy pixels retained after quality control, and dashed lines indicate the corresponding median values summarized in Table 1.

increase. Moreover, substantial spatial variability in τ persists within the individual flight legs, indicating pronounced local optical heterogeneity even within the increasingly connected downstream cloud fields.

https://doi.org/10.5194/egusphere-2026-6598
Preprint. Discussion started: 23 November 2026
© Author(s) 2026. CC BY 4.0 License.

To characterize the local organization of the quality-controlled liquid-cloud field, a retrieval-based local cloud fraction (LCF) is calculated as the fraction of pixels with a valid liquid-cloud retrieval within a moving window of approximately 2 km by 2 km. The LCF fields (not shown) are used below as a local measure of cloud organization when examining its relationship with ω_{e}^{*}.

3.2 Evolution of radiative and dynamical properties

The evolution of radiative effects and derived dynamical quantities across the downstream sequence of the flight legs is shown in Fig. 8. For convenience, the median values represented by the dashed lines in the histograms are summarized together with those of the observed and retrieved cloud properties in Table 1. While the cloud-top cooling rate $\zeta_{20\,\mathrm{m}}$ and the vertical distribution of radiative cooling represented by z_{c} exhibit substantial spatial variability, their median values show no monotonic downstream trend. In contrast, the radiatively derived entrainment velocity ω_{e}^{*} increases systematically along the downstream sequence, indicating that the radiative–dynamical response evolves more clearly than either radiative quantity considered individually.

Table 1. Median values of all quantities shown by the dashed lines in the histograms throughout Figs. 3, 7, and 8. The statistics include only cloudy pixels retained after the retrieval quality control and used in the subsequent quantitative analysis. Phase-suspect pixels, τ-saturated retrievals, and unresolved retrieval inconsistencies are excluded.

Quantity	Leg 4	Leg 3	Leg 2	Leg 1
R_{1250} (–)	0.39	0.44	0.38	0.37
T_{B} (°C)	-15.5	-15.4	-17.5	-16.8
τ (–)	9.1	16.0	9.6	9.4
r_{eff} (µm)	7.4	8.9	10.7	14.6
CTH (km)	1.00	1.25	1.35	1.50
$\Delta\theta_{\mathrm{inv}}$ (K)	3.9	3.7	3.2	2.9
$\zeta_{20\,\mathrm{m}}$ (K h^{-1})	-4.1	-4.8	-4.4	-4.5
z_{c} (km)	0.06	0.06	0.07	0.06
ω_{e}^{*} (mm s^{-1})	15.8	19.0	23.4	24.7

The changes in cloud morphology and microphysical properties are accompanied by pronounced spatial variability in cloud-top radiative cooling. Rather than varying uniformly across the cloud fields, $\zeta_{20\,\mathrm{m}}$ exhibits strong local contrasts, with regions of intense cooling occurring adjacent to substantially weaker cooling. These contrasts remain evident throughout all four flight legs, including within the more spatially connected cloud fields observed further downstream. Despite this pronounced spatial heterogeneity, the median cooling rates vary only moderately between the legs, ranging from $-4.1\,\mathrm{K\,h^{-1}}$ in Leg 4 to $-4.8\,\mathrm{K\,h^{-1}}$ in Leg 3, without a monotonic downstream trend.

Furthermore, z_{c} likewise exhibits substantial spatial variability, but its median value remains remarkably similar among the four flight legs. Median z_{c} values range only from approximately 0.06 km to 0.07 km, indicating that the characteristic vertical

https://doi.org/10.5194/egusphere-2026-6598
Preprint. Discussion started: 23 November 2026
© Author(s) 2026. CC BY 4.0 License.

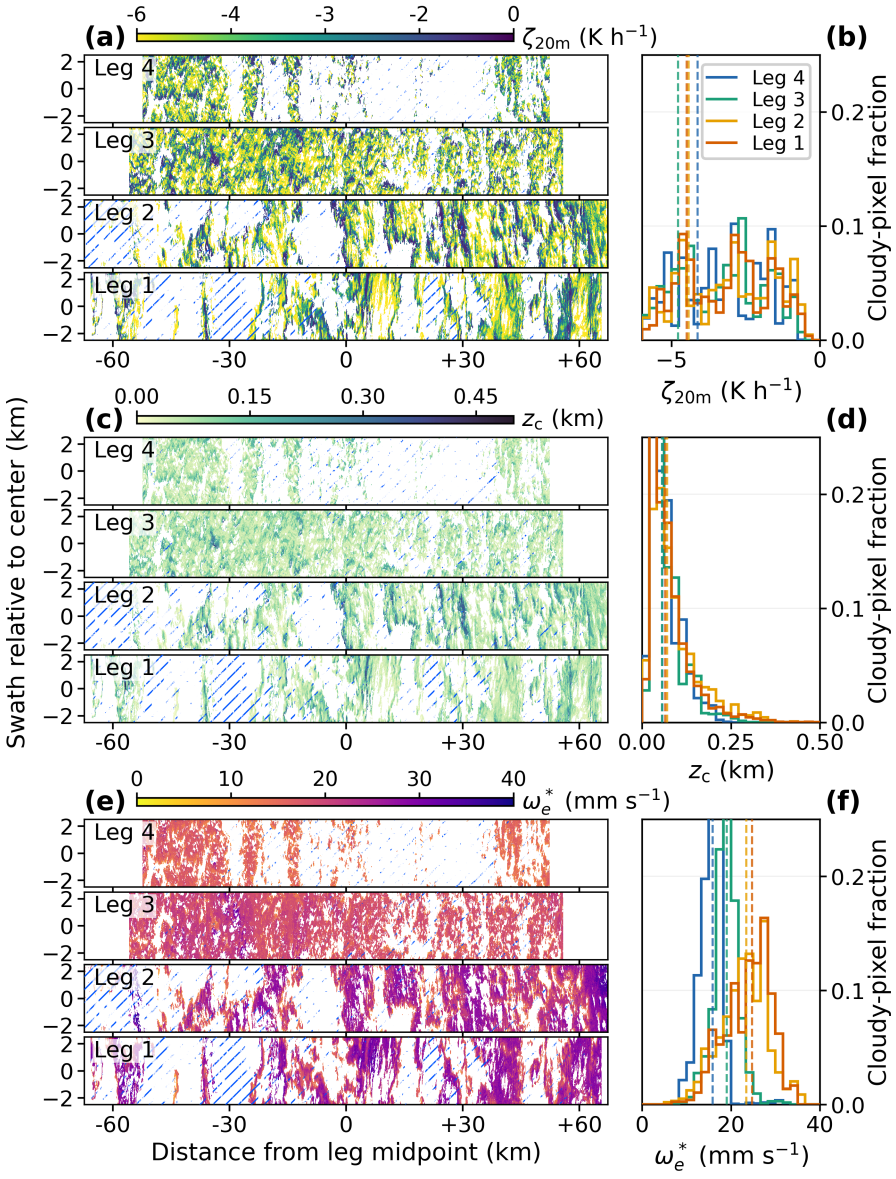

Figure 8. Like in Fig. 3, spatial distributions and corresponding frequency distributions of **(a, b)** $\zeta_{20\,\mathrm{m}}$, **(c, d)** z_c, and **(e, f)** ω_e^*, respectively. As in Fig. 7, dark blue hatched areas indicate cloudy pixels excluded by the retrieval quality control, while the corresponding histograms contain only retained retrieval pixels.

location of the radiative cooling relative to cloud top does not undergo a systematic downstream shift. Local differences in z_c nevertheless remain visible within the individual cloud fields, emphasizing that the vertical distribution of radiative cooling varies considerably on spatial scales smaller than those represented by the leg-wise statistics.

https://doi.org/10.5194/egusphere-2026-6598
Preprint. Discussion started: 23 November 2026
© Author(s) 2026. CC BY 4.0 License.

A much clearer downstream evolution emerges for the derived radiatively derived entrainment velocity ω_e^*. Its median value increases systematically from 15.8 mm s^{-1} in Leg 4 to 19.0 mm s^{-1} in Leg 3, 23.4 mm s^{-1} in Leg 2, and 24.7 mm s^{-1} in Leg 1. Spatially, elevated ω_e^* values are rather local features in the fragmented cloud field of Leg 4 but become more widespread within the increasingly connected downstream cloud fields. Thus, although neither $\zeta_{20\,\mathrm{m}}$ nor z_c exhibits a comparable monotonic change in its median value, their combined contribution together with the evolving inversion strength $\Delta\theta_{\mathrm{inv}}$ results in a pronounced downstream increase in the diagnosed radiatively derived entrainment velocity ω_e^*.

4 Relationships between cloud properties and ω_e^*

Bivariate relationships between ω_e^* and selected cloud microphysical and macrophysical quantities are summarized in Fig. 9. Because ω_e^* represents the central entrainment-related diagnostic in this study, it is shown consistently on the ordinate to facilitate comparison among the different cloud properties. Subsampled pixel data illustrate the underlying variability, while binned medians and interquartile ranges highlight systematic tendencies within the individual flight legs. Relationships are evident for all considered variables, although their strength, functional form, and absolute level differ substantially between the sampled cloud regimes.

The inversion strength is not included as an additional bivariate relationship in Fig. 9 because $\Delta\theta_{\mathrm{inv}}$ is represented by one dropsonde-derived value per flight leg rather than by a spatially resolved field. Nevertheless, $\Delta\theta_{\mathrm{inv}}$ exhibits a systematic downstream decrease from 3.87 K in Leg 4 to 3.70 K in Leg 3, 3.20 K in Leg 2, and 2.94 K in Leg 1 (Table 1). This progressive weakening of the inversion occurs together with the downstream increase in ω_e^* and, therefore, contributes to the systematic leg-to-leg differences in the diagnosed radiatively derived entrainment velocity.

Within the individual flight legs, ω_e^* generally increases with τ (Fig. 9a), although the strength of this relationship differs among the sampled cloud regimes. The strongest increase occurs at small to moderate optical thickness, whereas the binned medians tend to flatten at larger τ. As the cloud becomes optically thick in the thermal–infrared, its longwave emissivity approaches unity, such that further increases in τ produce progressively smaller changes in cloud-top thermal emission and, consequently, in radiative cooling (Lilly, 1968; Stevens, 2002; Wood, 2012). However, τ alone does not uniquely determine the radiative response, which also depends on the vertical distribution of liquid water and the geometrical structure of the cloud layer. The pronounced offsets between the flight legs further demonstrate that a given value of τ does not correspond to a unique value of ω_e^*. Thus, cloud optical thickness represents only one component of the radiative–dynamical state, while differences in cloud geometry, the vertical cooling distribution, and inversion strength modulate the absolute level of ω_e^* between the individual cloud regimes.

In contrast, the relationship between ω_e^* and r_{eff} is comparatively weak (Fig. 9b). Within the individual flight legs, the binned medians vary only slightly across most of the observed r_{eff} range, while pronounced offsets remain between the different cloud regimes. Thus, local variations in r_{eff} alone are only weakly associated with spatial variability in ω_e^* in the present case. The leg-to-leg separation instead suggests that differences in cloud optical and geometrical properties, radiative cooling, and inversion strength are more important for the absolute level of ω_e^* than local variations in r_{eff} alone.

https://doi.org/10.5194/egusphere-2026-6598
Preprint. Discussion started: 23 November 2026
© Author(s) 2026. CC BY 4.0 License.

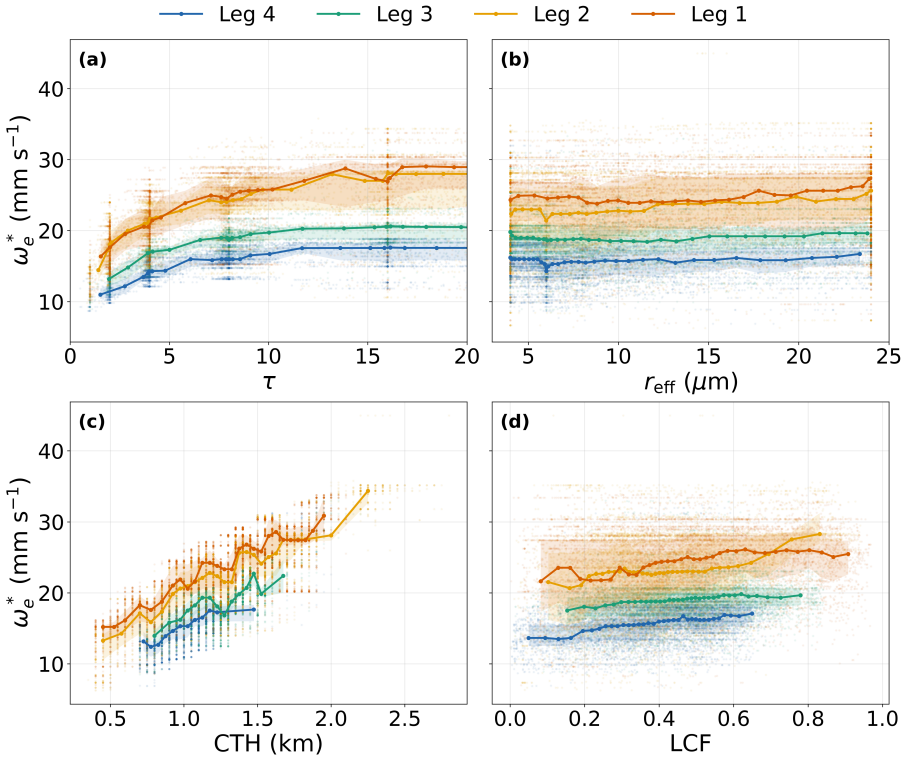

Figure 9. Bivariate relationships between ω_e^* and the selected cloud properties: **(a)** τ, **(b)** r_{eff}, **(c)** CTH, and **(d)** local cloud fraction (LCF). Faint points represent subsampled quality-controlled retrieval pixels. Colored lines show the binned medians of ω_e^* for each flight leg, and shaded areas indicate the corresponding interquartile ranges (25th–75th percentiles). The LCF is calculated from the fraction of valid liquid-cloud retrieval pixels within the local analysis window, excluding pixels removed by the retrieval quality control.

The clearest approximately monotonic relationship is found for CTH (Fig. 9c). In all four flight legs, higher cloud tops are generally associated with larger ω_e^*, although the magnitude of ω_e^* differs between legs. The positive relationship should not, however, be interpreted as evidence that higher cloud tops necessarily experience stronger cloud-top radiative cooling. As defined here, ω_e^* combines the cooling magnitude with the vertical distribution of radiative cooling through z_c and the thermodynamic resistance to entrainment represented by $\Delta\theta_{\mathrm{inv}}$. Similar CTH values can therefore correspond to substantially different ω_e^* values under different radiative and thermodynamic conditions. The leg-to-leg separation demonstrates that CTH is closely associated with the downstream evolution of ω_e^* but does not determine it independently.

The retrieval-based LCF also shows an overall positive association with ω_e^* (Fig. 9d), with generally lower LCF values in Legs 3 and 4 but a qualitatively similar relationship across all four legs. Importantly, LCF in the present analysis represents the local fraction of pixels with a valid liquid-cloud retrieval rather than the geometrical cloud fraction of all cloud phases. Pixels excluded by the retrieval quality control, including unresolved retrieval inconsistencies, some of which may be associated with three-dimensional radiative effects, are not counted towards the valid liquid-cloud fraction. Consequently, the retrieval-based

https://doi.org/10.5194/egusphere-2026-6598
Preprint. Discussion started: 23 November 2026
© Author(s) 2026. CC BY 4.0 License.

LCF does not necessarily approach unity even in spatially extensive cloud fields. Despite this methodological distinction, the systematic offsets between the flight legs remain evident. Comparable LCF values are associated with substantially different ω_e^* ranges in the upstream and downstream cloud regimes. Thus, the observed relationship cannot be attributed to cloud-field continuity alone but reflects concurrent changes in cloud geometry, microphysics, radiative cooling, and inversion strength.

The substantial spread of ω_e^* observed for comparable values of τ, CTH, or LCF further illustrates that no single cloud property uniquely determines the radiatively derived entrainment velocity. Although these cloud properties are associated with variations in the radiative state of the cloud field, ω_e^* additionally depends explicitly on the magnitude and vertical distribution of radiative cooling and on the inversion strength through $\Delta\theta_{\mathrm{inv}}$. Differences in these quantities between the sampled flight legs contribute to the systematic offsets between the individual cloud regimes, whereas the remaining spread within each leg reflects the substantial small-scale variability of the retrieved and simulated cloud-radiative properties.

Taken together, the bivariate relationships reveal a clear regime dependence. Differences between flight legs can influence relationships observed in the combined dataset, which may therefore differ from those found within individual legs. The CTH shows the clearest positive association with ω_e^*, while τ also exhibits a generally positive but non-linear relationship. The relationship with r_{eff} is comparatively weak, whereas the association with retrieval-based LCF varies among the cloud regimes. Because these cloud properties are physically interdependent and because ω_e^* is itself derived from the radiative cooling magnitude, cooling-centroid depth, and inversion strength, the bivariate relationships do not provide an independent attribution of causality or relative predictor importance. Instead, they demonstrate how the association of ω_e^* with cloud optical, geometrical, and organizational properties changes during the downstream evolution of the CAO cloud field. This behaviour is consistent with the interpretation of ω_e^* as a diagnostic quantity integrating radiative and thermodynamic controls on entrainment-related changes.

5 Conclusions

This study combines airborne remote-sensing observations from HALO-$(\mathcal{AC})^3$, dropsonde measurements, and broadband radiative-transfer simulations to investigate the downstream evolution of radiatively constrained entrainment potential in Arctic cold air outbreak (CAO) clouds south of Svalbard. Retrieved cloud microphysical and macrophysical properties were used to reconstruct representative profiles of cloud properties, from which radiative cooling profiles and the radiatively derived entrainment velocity ω_e^* were derived. The analysis provides an observationally constrained framework linking cloud properties and thermodynamic conditions to spatial variations in the radiative forcing relevant for cloud-top entrainment.

The observations reveal a systematic transition from fragmented and shallow upstream Arctic atmospheric boundary layer (ABL) cloud fields towards deeper and more spatially connected cloud structures farther downstream of the investigated CAO. This evolution is accompanied by pronounced changes in cloud microphysical and macrophysical properties and in the spatial organization of cloud-top radiative cooling. Although strong small-scale variability persists throughout all four flight legs, the derived ω_e^* increases systematically downstream, with median values ranging from 16 mm s^{-1} in Leg 4 to 25 mm s^{-1} in Leg 1.

https://doi.org/10.5194/egusphere-2026-6598
Preprint. Discussion started: 23 November 2026
© Author(s) 2026. CC BY 4.0 License.

The increase in ω_e^* occurs together with the broader evolution of the cloud and ABL state rather than reflecting a uniform change in cloud-top radiative cooling alone.

The bivariate analyses demonstrate that the correlation between ω_e^* and individual cloud properties differ among the sampled cloud regimes. Cloud-top height (CTH) shows the clearest positive correlation with ω_e^*, while cloud optical thickness (τ) exhibits a generally positive but non-linear relationship within the individual flight legs. In contrast, the correlation with cloud-droplet effective radius (r_{eff}) is comparatively weak. The retrieval-based local cloud fraction (LCF) shows an overall positive correlation with ω_e^*, with differences between legs primarily reflected in their offsets rather than clearly distinct slopes. Pronounced offsets between the flight legs remain for comparable values of the individual cloud properties, indicating that no single variable uniquely determines ω_e^*. Instead, the radiatively derived entrainment velocity reflects the combined influence of cloud optical and macrophysical properties, the magnitude and vertical distribution of radiative cooling, and the thermodynamic resistance to entrainment.

The proposed radiatively derived entrainment velocity is interpreted as a diagnostic measure of the radiatively constrained component of entrainment rather than an estimate of the actual entrainment rate. The magnitude of ω_e^* may be expected to approach the actual entrainment velocity most closely in cloud regimes where cloud-top turbulence is predominantly driven by radiative cooling and additional contributions from shear, surface-driven turbulence, precipitation, and independently varying evaporative effects are comparatively weak (Mellado, 2017; de Lozar and Mellado, 2015; Neggers et al., 2025). In the present CAO, these conditions cannot be assumed. An exploratory analysis of the representative dropsonde wind profiles reveals substantial differences in inversion-layer wind shear between the flight legs. The wind-vector jump is largest in Leg 1 (approximately $2.5\,\mathrm{m\,s^{-1}}$), compared with 0.5–$1.1\,\mathrm{m\,s^{-1}}$ in Legs 2–4. Correspondingly, Leg 1 exhibits the lowest bulk Richardson number (approximately 1.7), whereas values range from approximately 10 to 60 in the other legs. These differences suggest that conditions for shear-assisted mixing may be comparatively more favorable in Leg 1, although the contribution of wind shear to actual cloud-top entrainment cannot be quantified from these observations.

The propagated measurement, retrieval, and thermodynamic uncertainties result in combined median relative uncertainties of about 9–12 % among the four flight legs, corresponding to representative absolute uncertainties of approximately 1–3 $\mathrm{mm\,s^{-1}}$. Additional structural uncertainties arise from the idealized one-dimensional cloud reconstruction and radiative-transfer framework and are not included in these numerical uncertainty estimates. In particular, the retrieval assumes liquid-water, plane-parallel clouds, whereas the observations reveal localized ice-containing or mixed-phase cloud-top conditions as well as regions affected by three-dimensional cloud-radiative effects. Such pixels are excluded by the retrieval quality control and are not included in the quantitative analysis. Ice occurring below an apparently liquid water cloud top, however, cannot be fully identified by the available cloud-top observations and may introduce additional uncertainty. Therefore, the reported relationships apply specifically to the quality-controlled, liquid water cloud portion of the observed cloud fields, and the relative spatial variability and regime-dependent behaviour are considered more robust than the absolute magnitude of the radiatively derived entrainment velocity.

The identified regime dependence has implications for the representation of Arctic ABL clouds in numerical models. The coupling between cloud structure, radiative cooling, and entrainment-related dynamics cannot be represented solely through

https://doi.org/10.5194/egusphere-2026-6598
Preprint. Discussion started: 23 November 2026
© Author(s) 2026. CC BY 4.0 License.

a single cloud property or a universal relationship that is valid across different stages of CAO development. Models need to reproduce the evolving cloud and thermodynamic state that governs the radiative and thermodynamic conditions relevant for an entrainment-related response. Because entrainment influences cloud-top evaporation, turbulent mixing, and cloud-layer evolution, systematic changes in the radiatively constrained entrainment potential may contribute to the observed transformation of Arctic CAO cloud fields. Quantifying this contribution to the actual dynamical entrainment rate will require direct comparisons with turbulence observations and high-resolution simulations.

The present analysis focuses on the liquid water cloud component of an individual case study of a specific Arctic CAO evolution. Therefore, it does not establish the generality of the identified relationships across other CAO events or cloud regimes. The framework may be transferable to mixed-phase clouds, but its application to cloud regimes with substantial ice contributions would require extending the retrieval and radiative-transfer representation to account explicitly for cloud phase and the vertical partitioning of liquid water and ice. More generally, the framework may also be applicable to other boundary-layer cloud regimes in which cloud-top radiative cooling contributes substantially to turbulence and entrainment. Extending the framework to additional CAO events, other boundary-layer cloud regimes, and mixed-phase conditions, while accounting for three-dimensional radiative effects and combining the remote-sensing diagnostics with direct dynamical constraints, will be important next steps.

Data availability. The data used in this study are available from the PANGAEA database, more specifically the VELOX brightness temperature from Schäfer et al. (2023), the specMACS radiance fields from Weber et al. (2024b), and the atmospheric profiles from the dropsonde measurements by George et al. (2024). The lidar data from WALES, which are used to correct the retrieved cloud-top height are provided by Wirth and Groß (2024). Positional data and flight tracks are available from Ehrlich et al. (2024). All further processed and/or simulated data are available upon request.

Author contributions. MS was the primary author of the paper. MWe designed the airborne experiments, which were performed by MS, AE, BK, AW, MWi and MWe. Simulations were performed by MS, JM and SR. MS, AE, JM, SR, and EJ analysed the observations and simulations. BK provided the Lagrangian trajectory analysis. AW and MWi provided guidance for the analysis of the specMACS and WALES data. AE, MWe, JM, SR, EJ, and MDS provided technical guidance throughout the main analysis. All authors contributed to the interpretation of results and wrote the paper.

Competing interests. The authors declare that they have no conflict of interest.

Acknowledgements. We gratefully acknowledge the funding by the Deutsche Forschungsgemeinschaft (DFG, German Research Foundation) – Project Number 268020496 – TRR 172, within the framework of the Transregional Collaborative Research Center “ArctiC Amplification:

https://doi.org/10.5194/egusphere-2026-6598
Preprint. Discussion started: 23 November 2026
© Author(s) 2026. CC BY 4.0 License.



Climate Relevant Atmospheric and SurfaCe Processes, and Feedback Mechanisms $(AC)^3$". Within $(AC)^3$, MDS was supported by a Mercator Fellowship and by NOAA cooperative agreement NA22OAR4320151. We are further grateful for funding of the project WE 1900/38-1 by the DFG within the framework of the Priority Programme SPP 1294 to promote research with HALO. We thank the crews and the technicians of the German Aerospace Center (Deutsches Luft und Raumfahrtzentrum, DLR) for excellent technical and logistical support. This publication was supported by the Open Access Publishing Fund of Leipzig University.

https://doi.org/10.5194/egusphere-2026-6598
Preprint. Discussion started: 23 November 2026
© Author(s) 2026. CC BY 4.0 License.

References

Becker, S., Ehrlich, A., Schäfer, M., and Wendisch, M.: Quantifying the impact of solar zenith angle, cloud optical thickness, and surface albedo on the solar radiative effect of Arctic low-level clouds over open ocean and sea ice, *Atmos. Chem. Phys.*, **25**, 12831–12842, https://doi.org/10.5194/acp-25-12831-2025, 2025.

Boers, R., de Laat, A. T., Stein Zweers, D. C., and Dirksen, R. J.: Lifting potential of solar-heated aerosol layers, *Geophys. Res. Lett.*, **37**, L24802, https://doi.org/10.1029/2010GL045171, 2010.

Bretherton, C. S., and Wyant, M. C.: Moisture transport, lower-tropospheric stability, and decoupling of cloud-topped boundary layers, *J. Atmos. Sci.*, **54**, 148–167, https://doi.org/10.1175/1520-0469(1997)054<0148:MTLTSA>2.0.CO;2, 1997.

Brümmer, B.: Roll and Cell Convection in Wintertime Arctic Cold-Air Outbreaks, *J. Atmos. Sci.*, **56**, 2613–2636, https://doi.org/10.1175/1520-0469(1999)056<2613:RACCIW>2.0.CO;2, 1999.

Ceppi, P., Myers, T. A., Nowack, P., Wall, C. J., and Zelinka, M. D.: Implications of a pervasive climate model bias for low-cloud feedback, *Geophys. Res. Lett.*, **51**, e2024GL110525, https://doi.org/10.1029/2024GL110525, 2024.

Chechin, D. G., Lüpkes, C., Hartmann, J., Ehrlich, A., and Wendisch, M.: Turbulent structure of the Arctic boundary layer in early summer driven by stability, wind shear and cloud-top radiative cooling: ACLOUD airborne observations, *Atmos. Chem. Phys.*, **23**, 4685–4707, https://doi.org/10.5194/acp-23-4685-2023, 2023.

de Lozar, A. and Mellado, J. P.: Evaporative cooling amplification of the entrainment velocity in radiatively driven stratocumulus, *Geophys. Res. Lett.*, **42**, 7223–7229, https://doi.org/10.1002/2015GL065529, 2015.

Egerer, U., Gottschalk, M., Siebert, H., Ehrlich, A., and Wendisch, M.: The new BELUGA setup for collocated turbulence and radiation measurements using a tethered balloon: first applications in the cloudy Arctic boundary layer, *Atmos. Meas. Tech.*, **12**, 4019–4038, https://doi.org/10.5194/amt-12-4019-2019, 2019.

Ehrlich, A., Bierwirth, E., Wendisch, M., Gayet, J.-F., Mioche, G., Lampert, A., and Heintzenberg, J.: Cloud phase identification of Arctic boundary-layer clouds from airborne spectral reflection measurements: test of three approaches, *Atmos. Chem. Phys.*, **8**, 7493–7505, https://doi.org/10.5194/acp-8-7493-2008, 2008.

Ehrlich, A., Crewell, S., Wendisch, M., Giez, A., Zöger, M., Mallaun, C., and Nenakhov, V.: Master tracks of the HALO research aircraft during the HALO–(AC)^3 field campaign in 1 Hz temporal resolution [dataset publication series], *PANGAEA*, https://doi.org/10.1594/PANGAEA.967299, 2024.

Ehrlich, A., Crewell, S., Herber, A., Klingebiel, M., Lüpkes, C., Mech, M., Becker, S., Borrmann, S., Bozem, H., Buschmann, M., Clemen, H.-C., De La Torre Castro, E., Dorff, H., Dupuy, R., Eppers, O., Ewald, F., George, G., Giez, A., Grawe, S., Gourbeyre, C., Hartmann, J., Jäkel, E., Joppe, P., Jourdan, O., Jurányi, Z., Kirbus, B., Lucke, J., Luebke, A. E., Maahn, M., Maherndl, N., Mallaun, C., Mayer, J., Mertes, S., Mioche, G., Moser, M., Müller, H., Pörtge, V., Risse, N., Roberts, G., Rosenburg, S., Röttenbacher, J., Schäfer, M., Schaefer, J., Schäfler, A., Schirmacher, I., Schneider, J., Schnitt, S., Stratmann, F., Tatzelt, C., Voigt, C., Walbröl, A., Weber, A., Wetzel, B., Wirth, M., and Wendisch, M.: A comprehensive in situ and remote sensing data set collected during the HALO–(AC)^3 aircraft campaign, *Earth Syst. Sci. Data*, **17**, 1295–1328, https://doi.org/10.5194/essd-17-1295-2025, 2025.

Ewald, F., Kölling, T., Baumgartner, A., Zinner, T., and Mayer, B.: Design and characterization of specMACS, a multipurpose hyperspectral cloud and sky imager, *Atmos. Meas. Tech.*, **9**, 2015–2042, https://doi.org/10.5194/amt-9-2015-2016, 2016.

George, G., Luebke, A. E., Klingebiel, M., Mech, M., and Ehrlich, A.: Dropsonde measurements from HALO and POLAR 5 during HALO–(AC)^3 in 2022 [dataset bundled publication], *PANGAEA*, https://doi.org/10.1594/PANGAEA.968891, 2024.

https://doi.org/10.5194/egusphere-2026-6598
Preprint. Discussion started: 23 November 2026
© Author(s) 2026. CC BY 4.0 License.

Gryschka, M., Drüe, C., Etling, D., and Raasch, S.: On the influence of sea-ice inhomogeneities onto roll convection in cold-air outbreaks, *Geophys. Res. Lett.*, **35**, L23804, https://doi.org/10.1029/2008GL035845, 2008.

Gryschka, M., Fricke, J., and Raasch, S.: On the impact of forced roll convection on vertical turbulent transport in cold air outbreaks, *J. Geophys. Res. Atmos.*, **119**, 12513–12532, https://doi.org/10.1002/2014JD022160, 2014.

Kirbus, B., Chylik, J., Ehrlich, A., Becker, S., Schäfer, M., Neggers, R., and Wendisch, M.: Analysis of an Arctic cold air outbreak during autumn and related air mass transformations forced by surface changes and advection in higher altitudes, *Elementa: Science of the Anthropocene*, **11**(1), 00079, https://doi.org/10.1525/elementa.2023.00079, 2023.

Kirbus, B., Schirmacher, I., Klingebiel, M., Schäfer, M., Ehrlich, A., Slättberg, N., Lucke, J., Moser, M., Müller, H., and Wendisch, M.: Thermodynamic and cloud evolution in a cold-air outbreak during HALO-$(AC)^3$: quasi-Lagrangian observations compared to the ERA5 and CARRA reanalyses, *Atmos. Chem. Phys.*, **24**, 3883–3904, https://doi.org/10.5194/acp-24-3883-2024, 2024.

Klingebiel, M., Ehrlich, A., Gryschka, M., Risse, N., Maherndl, N., Schirmacher, I., Rosenburg, S., Hörnig, S., Moser, M., Jäkel, E., Schäfer, M., Deneke, H., Mech, M., Voigt, C., and Wendisch, M.: Airborne observations of cloud properties during their evolution from organized streets to isotropic cloud structures along an Arctic cold-air outbreak, *Atmos. Chem. Phys.*, **25**, 9787–9801, https://doi.org/10.5194/acp-25-9787-2025, 2025.

Krautstrunk, M. and Giez, A.: The Transition From FALCON to HALO Era Airborne Atmospheric Research, in: *Atmospheric Physics*, edited by: Schumann, U., Research Topics in Aerospace, Springer, Berlin, Heidelberg, 609–624, https://doi.org/10.1007/978-3-642-30183-4_37, 2012.

La, I., Shaw, R. A., Siebert, H., Ehrlich, A., Yeom, J. M., and Yum, S. S.: Cloud-top entrainment instability in marine stratocumulus clouds: Observational evidence from collocated microphysical, turbulence, and radiation measurements, *J. Geophys. Res. Atmos.*, **130**, e2025JD044582, https://doi.org/10.1029/2025JD044582, 2025.

Lilly, D. K.: Models of cloud-topped mixed layers under a strong inversion, *Q. J. R. Meteorol. Soc.*, **94**, 292–309, https://doi.org/10.1002/qj.49709440106, 1968.

Lonardi, M., Pilz, C., Akansu, E. F., Dahlke, S., Egerer, U., Ehrlich, A., Griesche, H., Heymsfield, A. J., Kirbus, B., Schmitt, C. G., Shupe, M. D., Siebert, H., Wehner, B., and Wendisch, M.: Tethered balloon-borne profile measurements of atmospheric properties in the cloudy atmospheric boundary layer over the Arctic sea ice during MOSAiC: Overview and first results, *Elementa: Science of the Anthropocene*, **10**(1), 000120, https://doi.org/10.1525/elementa.2021.000120, 2022.

Lonardi, M., Akansu, E. F., Ehrlich, A., Mazzola, M., Pilz, C., Shupe, M. D., Siebert, H., and Wendisch, M.: Tethered balloon-borne observations of thermal-infrared irradiance and cooling rate profiles in the Arctic atmospheric boundary layer, *Atmos. Chem. Phys.*, **24**, 1961–1978, https://doi.org/10.5194/acp-24-1961-2024, 2024.

Lloyd, G., Choularton, T. W., Bower, K. N., Crosier, J., Jones, H., Dorsey, J. R., Gallagher, M. W., Connolly, P., Kirchgaessner, A. C. R., and Lachlan-Cope, T.: Observations and comparisons of cloud microphysical properties in spring and summertime Arctic stratocumulus clouds during the ACCACIA campaign, *Atmos. Chem. Phys.*, **15**, 3719–3737, https://doi.org/10.5194/acp-15-3719-2015, 2015.

Mellado, J. P.: Cloud-Top Entrainment in Stratocumulus Clouds, *Annu. Rev. Fluid Mech.*, **49**, 145–169, https://doi.org/10.1146/annurev-fluid-010816-060231, 2017.

Mitra, A. and Ghate, V. P.: Towards retrieving cloud top entrainment velocities from MISR cloud motion vectors, *Atmos. Meas. Tech.*, **19**, 2025–2045, https://doi.org/10.5194/amt-19-2025-2026, 2026.

https://doi.org/10.5194/egusphere-2026-6598
Preprint. Discussion started: 23 November 2026
© Author(s) 2026. CC BY 4.0 License.

MODIS Characterization Support Team (MCST): MOD02QKM MODIS/Terra calibrated radiances 5-min L1B swath 250 m, NASA Level-1 and Atmosphere Archive & Distribution System Distributed Active Archive Center (LAADS DAAC), https://doi.org/10.5067/MODIS/MOD02QKM.061, last access: 11 May 2026, 2017.

Morrison, H., de Boer, G., Feingold, G., Harrington, J., Shupe, M. D., and Sulia, K.: Resilience of persistent Arctic mixed-phase clouds, *Nature Geosci.*, **5**(1), 11–17, https://doi.org/10.1038/ngeo1332, 2012.

NASA MODIS Adaptive Processing System: MODIS/Terra Cloud Product L2, https://doi.org/10.5067/MODIS/MOD06_L2.061, 2021.

Neggers, R. A. J., Chylik, J., and Schnierstein, N.: The entrainment efficiency of persistent Arctic mixed-phase clouds as inferred from daily large-eddy simulations during the MOSAiC drift, *J. Atmos. Sci.*, **82**, 1195–1213, https://doi.org/10.1175/JAS-D-24-0188.1, 2025.

Platnick, S., King, M. D., Ackerman, S. A., Menzel, W. P., Baum, B. A., Riedi, J. C., and Frey, R. A.: The MODIS cloud products: algorithms and examples from Terra, *IEEE Trans. Geosci. Remote Sens.*, **41**(2), 459–473, https://doi.org/10.1109/TGRS.2002.808301, 2003.

Ren, T., Yang, P., Huang, X., Chen, X., and Shen, Z.: Enhanced cloud top longwave radiative cooling due to the effect of horizontal radiative transfer in the stratocumulus to trade cumulus transition regime, *Geophys. Res. Lett.*, **50**, e2023GL106076, https://doi.org/10.1029/2023GL106076, 2023.

Schäfer, M., Wolf, K., Ehrlich, A., Hallbauer, C., Jäkel, E., Jansen, F., Luebke, A. E., Müller, J., Thoböll, J., Röschenthaler, T., Stevens, B., and Wendisch, M.: VELOX – a new thermal infrared imager for airborne remote sensing of cloud and surface properties, *Atmos. Meas. Tech.*, **15**, 1491–1509, https://doi.org/10.5194/amt-15-1491-2022, 2022.

Schäfer, M., Rosenburg, S., Ehrlich, A., Röttenbacher, J., and Wendisch, M.: Two-dimensional cloud-top and surface brightness temperature with 1 Hz temporal resolution derived at flight altitude from VELOX during the HALO–(AC)^3 field campaign [dataset publication series], *PANGAEA*, https://doi.org/10.1594/PANGAEA.963401, 2023.

Sedlar, J., Shupe, M. D., and Tjernström, M.: On the Relationship between Thermodynamic Structure and Cloud Top, and Its Climate Significance in the Arctic, *J. Climate*, **25**, 2374–2393, https://doi.org/10.1175/JCLI-D-11-00186.1, 2012.

Shupe, M. D.: Clouds at Arctic atmospheric observatories. Part II: Thermodynamic phase characteristics, *J. Appl. Meteorol. Climatol.*, **50**(3), 645–661, https://doi.org/10.1175/2010JAMC2468.1, 2011.

Shupe, M. D., Persson, P. O. G., Brooks, I. M., Tjernström, M., Sedlar, J., Mauritsen, T., Sjogren, S., and Leck, C.: Cloud and boundary layer interactions over the Arctic sea ice in late summer, *Atmos. Chem. Phys.*, **13**, 9379–9399, https://doi.org/10.5194/acp-13-9379-2013, 2013.

Spreen, G., Kaleschke, L., and Heygster, G.: Sea ice remote sensing using AMSR–E 89 GHz channels, *J. Geophys. Res.*, **113**, C02S03, https://doi.org/10.1029/2005JC003384, 2008.

Sprenger, M. and Wernli, H.: The LAGRANTO Lagrangian analysis tool – version 2.0, *Geosci. Model Dev.*, **8**, 2569–2586, https://doi.org/10.5194/gmd-8-2569-2015, 2015.

Stevens, B.: Entrainment in stratocumulus-topped mixed layers, *Q. J. R. Meteorol. Soc.*, **128**, 2663–2690, https://doi.org/10.1256/qj.01.202, 2002.

Turner, D. D., Shupe, M. D., and Zwink, A. B.: Characteristic atmospheric radiative heating rate profiles in Arctic clouds as observed at Barrow, Alaska, *J. Appl. Meteor. Climatol.*, **57**, 953–968, https://doi.org/10.1175/JAMC-D-17-0252.1, 2018.

Walbröl, A., Michaelis, J., Becker, S., Dorff, H., Ebell, K., Gorodetskaya, I., Heinold, B., Kirbus, B., Lauer, M., Maherndl, N., Maturilli, M., Mayer, J., Müller, H., Neggers, R. A. J., Paulus, F. M., Röttenbacher, J., Rückert, J. E., Schirmacher, I., Slättberg, N., Ehrlich, A., Wendisch, M., and Crewell, S.: Contrasting extremely warm and long-lasting cold air anomalies in the North Atlantic sector of the Arctic during the HALO–(AC)^3 campaign, *Atmos. Chem. Phys.*, **24**, 8007–8029, https://doi.org/10.5194/acp-24-8007-2024, 2024.

https://doi.org/10.5194/egusphere-2026-6598
Preprint. Discussion started: 23 November 2026
© Author(s) 2026. CC BY 4.0 License.

Weber, A., Kölling, T., Pörtge, V., Baumgartner, A., Rammeloo, C., Zinner, T., and Mayer, B.: Polarization upgrade of specMACS: calibration and characterization of the 2D RGB polarization-resolving cameras, *Atmos. Meas. Tech.*, **17**, 1419–1439, https://doi.org/10.5194/amt-17-1419-2024, 2024.

Weber, A., Pörtge, V., Zinner, T., and Mayer, B.: Spectral radiance measurements with the hyperspectral and polarized imaging system specMACS during the HALO–(AC)^3 field campaign [dataset], *PANGAEA*, https://doi.org/10.1594/PANGAEA.966992, 2024.

Wendisch, M., Brückner, M., Burrows, J. P., Crewell, S., Dethloff, K., Ebell, K., Lüpkes, C., Macke, A., Notholt, J., Quaas, J., Rinke, A., and Tegen, I.: Understanding causes and effects of rapid warming in the Arctic, *Eos*, **98**, https://doi.org/10.1029/2017EO064803, 2017.

Wendisch, M., Brückner, M., Crewell, S., Ehrlich, A., Notholt, J., Lüpkes, C., Macke, A., Burrows, J. P., Rinke, A., Quaas, J., Maturilli, M., Schemann, V., Shupe, M. D., Akansu, E. F., Barrientos-Velasco, C., Bärfuss, K., Blechschmidt, A.-M., Block, K., Bougoudis, I., Bozem, H., Böckmann, C., Bracher, A., Bresson, H., Bretschneider, L., Buschmann, M., Chechin, D. G., Chylik, J., Dahlke, S., Deneke, H., Dethloff, K., Donth, T., Dorn, W., Dupuy, R., Ebell, K., Egerer, U., Engelmann, R., Eppers, O., Gerdes, R., Gierens, R., Gorodetskaya, I. V., Gottschalk, M., Griesche, H., Gryanik, V. M., Handorf, D., Harm-Altstädter, B., Hartmann, J., Hartmann, M., Heinold, B., Herber, A., Herrmann, H., Heygster, G., Höschel, I., Hofmann, Z., Hölemann, J., Hünerbein, A., Jafariserajehlou, S., Jäkel, E., Jacobi, C., Janout, M., Jansen, F., Jourdan, O., Jurányi, Z., Kalesse-Los, H., Kanzow, T., Käthner, R., Kliesch, L. L., Klingebiel, M., Knudsen, E. M., Kovács, T., Körtke, W., Krampe, D., Kretzschmar, J., Kreyling, D., Kulla, B., Kunkel, D., Lampert, A., Lauer, M., Lelli, L., von Lerber, A., Linke, O., Löhnert, U., Lonardi, M., Losa, S. N., Losch, M., Maahn, M., Mech, M., Mei, L., Mertes, S., Metzner, E., Mewes, D., Michaelis, J., Mioche, G., Moser, M., Nakoudi, K., Neggers, R., Neuber, R., Nomokonova, T., Oelker, J., Papakonstantinou-Presvelou, I., Pätzold, F., Pefanis, V., Pohl, C., van Pinxteren, M., Radovan, A., Rhein, M., Rex, M., Richter, A., Risse, N., Ritter, C., Rostosky, P., Rozanov, V. V., Ruiz Donoso, E., Saavedra Garfias, P., Salzmann, M., Schacht, J., Schäfer, M., Schneider, J., Schnierstein, N., Seifert, P., Seo, S., Siebert, H., Soppa, M. A., Spreen, G., Stachlewska, I. S., Stapf, J., Stratmann, F., Tegen, I., Viceto, C., Voigt, C., Vountas, M., Walbröl, A., Walter, M., Wehner, B., Wex, H., Willmes, S., Zanatta, M., and Zeppenfeld, S.: Atmospheric and surface processes, and feedback mechanisms determining Arctic amplification: A review of first results and prospects of the (AC)^3 project, *Bull. Am. Meteorol. Soc.*, **104**(1), E208–E242, https://doi.org/10.1175/BAMS-D-21-0218.1, 2023.

Wendisch, M., Crewell, S., Ehrlich, A., Herber, A., Kirbus, B., Lüpkes, C., Mech, M., Abel, S. J., Akansu, E. F., Ament, F., Aubry, C., Becker, S., Borrmann, S., Bozem, H., Brückner, M., Clemen, H.-C., Dahlke, S., Dekoutsidis, G., Delanoë, J., De La Torre Castro, E., Dorff, H., Dupuy, R., Eppers, O., Ewald, F., George, G., Gorodetskaya, I. V., Grawe, S., Groß, S., Hartmann, J., Henning, S., Hirsch, L., Jäkel, E., Joppe, P., Jourdan, O., Jurányi, Z., Karalis, M., Kellermann, M., Klingebiel, M., Lonardi, M., Lucke, J., Luebke, A. E., Maahn, M., Maherndl, N., Maturilli, M., Mayer, B., Mayer, J., Mertes, S., Michaelis, J., Michalkov, M., Mioche, G., Moser, M., Müller, H., Neggers, R., Ori, D., Paul, D., Paulus, F. M., Pilz, C., Pithan, F., Pöhlker, M., Pörtge, V., Ringel, M., Risse, N., Roberts, G. C., Rosenburg, S., Röttenbacher, J., Rückert, J., Schäfer, M., Schaefer, J., Schemann, V., Schirmacher, I., Schmidt, J., Schmidt, S., Schneider, J., Schnitt, S., Schwarz, A., Siebert, H., Sodemann, H., Sperzel, T., Spreen, G., Stevens, B., Stratmann, F., Svensson, G., Tatzelt, C., Tuch, T., Vihma, T., Voigt, C., Volkmer, L., Walbröl, A., Weber, A., Wehner, B., Wetzel, B., Wirth, M., and Zinner, T.: Overview: quasi-Lagrangian observations of Arctic air mass transformations – introduction and initial results of the HALO–(AC)^3 aircraft campaign, *Atmos. Chem. Phys.*, **24**, 8865–8892, https://doi.org/10.5194/acp-24-8865-2024, 2024.

Wendisch, M., Kirbus, B., Ori, D., Shupe, M. D., Crewell, S., Sodemann, H., and Schemann, V.: Observed and modeled Arctic airmass transformations during warm air intrusions and cold air outbreaks, *Atmos. Chem. Phys.*, **25**, 15047–15076, https://doi.org/10.5194/acp-25-15047-2025, 2025.

https://doi.org/10.5194/egusphere-2026-6598
Preprint. Discussion started: 23 November 2026
© Author(s) 2026. CC BY 4.0 License.



Wirth, M. and Groß, S.: Aircraft measurements of backscatter ratio, particle depolarization and water vapour molecular density profiles over Arctic sea ice and ocean during the HALO–(AC)^3 campaign in spring 2022 [dataset], *PANGAEA*, https://doi.org/10.1594/PANGAEA.967086, 2024.

Wood, R.: Stratocumulus clouds, *Mon. Wea. Rev.*, **140**, 2373–2423, https://doi.org/10.1175/MWR-D-11-00121.1, 2012.

Zheng, Y., Zhu, Y., Rosenfeld, D., and Li, Z.: Climatology of cloud-top radiative cooling in marine shallow clouds, *Geophys. Res. Lett.*, **48**, e2021GL094676, https://doi.org/10.1029/2021GL094676, 2021.